

The Design of a Reflectance Spectrometer and its Calibration using SrTiO_3

by

J.R.S. (Rob) Klassen

B.Sc. (Hons. Phys.), Brock University, 2002

A THESIS SUBMITTED IN PARTIAL FULFILMENT OF
THE REQUIREMENTS FOR THE DEGREE OF

MASTER OF SCIENCE

in

The Faculty of Mathematics and Sciences

Department of Physics



BROCK UNIVERSITY

September 1, 2004

2004 © J.R.S. (Rob) Klassen

Abstract

A new Ultra-High Vacuum (UHV) reflectance spectrometer was successfully designed, making use of a Janis Industries ST-400 sample cryostat, IR Labs bolometer, and Brüker IFS 66 v/S spectrometer. Two of the noteworthy features include an *in situ* gold evaporator and internal reference path, both of which allow for the experiment to progress with a completely undisturbed sample position. As tested, the system was designed to operate between 4.2 K and 325 K over a frequency range of 60 – 670 cm^{-1} . This frequency range can easily be extended through the addition of applicable detectors.

Tests were performed on SrTiO_3 , a highly ionic incipient ferroelectric insulator with a well known reflectance. The presence and temperature dependence of the lowest frequency “soft” mode were measured, as was the presence of the other two infrared modes. During the structural phase transition from cubic to tetragonal perovskite, the splitting of the second phonon mode was also observed. All of the collected data indicate good agreement with previous measurements, with a minor discrepancy between the actual and recorded sample temperatures.

Contents

Abstract	ii
Contents	iii
List of Tables	v
List of Figures	vi
Acknowledgements	vii
1 Introduction	1
1.1 Design Goals	1
1.2 SrTiO_3	2
2 Experimental Design	6
2.1 Overview	6
2.2 Optics	7
2.2.1 The Optical Table	9
2.3 Sample Chamber	10
2.4 Detector	13
3 Theory	15
3.1 Overview	15
3.2 Fourier-Transform Spectroscopy	16
3.2.1 Optical Constants of Solids	19
3.3 Lorentz Model	20
3.4 Factorized Dielectric Model	23
3.5 Lyddane-Sachs-Teller (LST) Relationship	26
3.6 Soft-Mode Behaviour	28
3.7 SrTiO_3 Lattice Dynamics	29
4 Measurements	33
4.1 Previous Reflectance Measurements	33
4.2 New Reflectance Measurements	33
4.2.1 March 25 Measurements	34
4.2.2 June 10 Measurements	36
5 Conclusions	43

Bibliography	45
-------------------------------	-----------

List of Tables

2.1	Process followed to obtain reflectance from collected data	6
2.2	Frequency ranges of the different optical components	8
4.1	Parameters found during fits of the factorized dielectric function.	40

List of Figures

1.1	Cubic-Perovskite Structure	2
1.2	Oxygen tetrahedron rotation	3
1.3	Plot of the dielectric susceptibility above T_c	4
1.4	Low temperature dielectric behaviour	5
2.1	Overview of the Experimental Components	7
2.2	Brüker IFS 66v/S Spectrometer	8
2.3	Optical Table & Light Paths	10
2.4	Cryostat adapter wedge	11
2.5	Differential Pumping Unit	12
2.6	Gold Evaporator	12
2.7	Schematic of a typical Bolometer	14
3.1	Power Spectrum & Interferogram	15
3.2	Michelson Interferometer	16
3.3	Typical relationship between $I(x)$ (labelled $g(x)$) and $s(x)$	18
3.4	Theoretically produced $n(\omega)$ and $k(\omega)$ (left), and $R(\omega)$ (right) for a single Lorentz oscillator centred about 4 eV	24
3.5	Comparison of the Lorentz and Factorized Dielectric models	25
3.6	Plots showing ω_{LO} and ω_{TO} versus k for both Ge (left) and KBr (right)	27
3.7	Previous measurements of the temperature dependence of the “soft” phonon mode	29
3.8	Plots of the soft-mode frequency versus applied electric field at 8 K (top), 40 K (middle), and 77 K (bottom).	30
3.9	Depictions of the stretching, bending, IR inactive, and external vibrational modes for a SrTiO_3 crystal	31
4.1	Previous Reflectance Work	34
4.2	300 K gold intermediate ratios	35
4.3	300 K Reflectance measurements	36
4.4	Reflectance at 10, 150, and 300 K	37
4.5	Summary of Reflectance Data and Fits	39
4.6	Plot of Ω_s^2 vs. T	41

Acknowledgements

Thank-you to Dr. Crandles for accepting me as a student (again) and allowing me to have creative freedom for many of the designs. As in the past, you have provided me guidance, assistance, and conversation. The entire Physics department has played a part in laying the groundwork for this project.

Much of the work behind this thesis was performed by the machine shop. Thanks to Roland, Steve, Art, Matt, and Mike for their “if you can draw it, we can build it” attitude. Your guidance and insight into the design/build process has been invaluable. Thank-you also for the opportunity to program and machine one of my own pieces.

Thanks also to Sudhakar and other members of the department for providing me with company in the lab, and relief from the monotony of data collection.

I would like to thank my parents (John and Janice), family, and friends for providing me with the encouragement to continue. The amount of stress you have relieved over the past two years is immeasurable.

Chapter 1

Introduction

Reflectance spectroscopy has provided many insights into the intrinsic properties of materials. The major goal of this MSc project was the design and implementation of a new reflectance spectrometer. Although the effectiveness of the newly designed system could have been tested with any well documented material, it was believed that SrTiO_3 would provide suitable interest in the frequency range used.

1.1 Design Goals

The initial goal in mind was to design a system which allowed light of a known frequency to strike a detector after reflecting off a sample at near-normal incidence, while at the same time controlling the temperature of the sample. In order to reduce sample contamination by oxidation or ice condensation, the sample chamber was chosen to operate in an ultra-high vacuum (UHV). In order to obtain UHV pressures while allowing light to enter the sample chamber, a differential pumping system was used to seal the optical window, as will be discussed later. Temperature controls were added, allowing for an effective range of sample temperatures from 4.2 K to 325 K.

Of great importance is the ability of the system to maintain sample position at all times throughout the experiment. Failure to do so would result in changes to the measured spectra over the course of an experiment. This was achieved through the use of a reference path which did not require the sample to be moved in any way (unlike many other systems employed in such measurements). For similar reasons, the system made use of an in-situ gold evaporation device which allowed for the necessary deposition of gold, leaving the sample undisturbed.

As tested, the system is now capable of reflectance measurements in the $60 - 670 \text{ cm}^{-1}$ range.

With a minimal amount of work, this range may be extended from 40 cm^{-1} to $45,000\text{ cm}^{-1}$, by the addition of different light sources, beamsplitters, and detectors to the system.

In order to determine whether the system was effective, tests were conducted on SrTiO_3 which has a well-known and temperature dependent reflectance spectrum.

1.2 SrTiO_3

SrTiO_3 is known to crystallize in a Cubic-Perovskite structure for temperatures above 110 K. In the perovskite unit cell, the central titanium atom is surrounded by both an octahedron of oxygen atoms and a cube of strontium atoms as shown in Figure 1.1. Below 110 K, a reversible structural

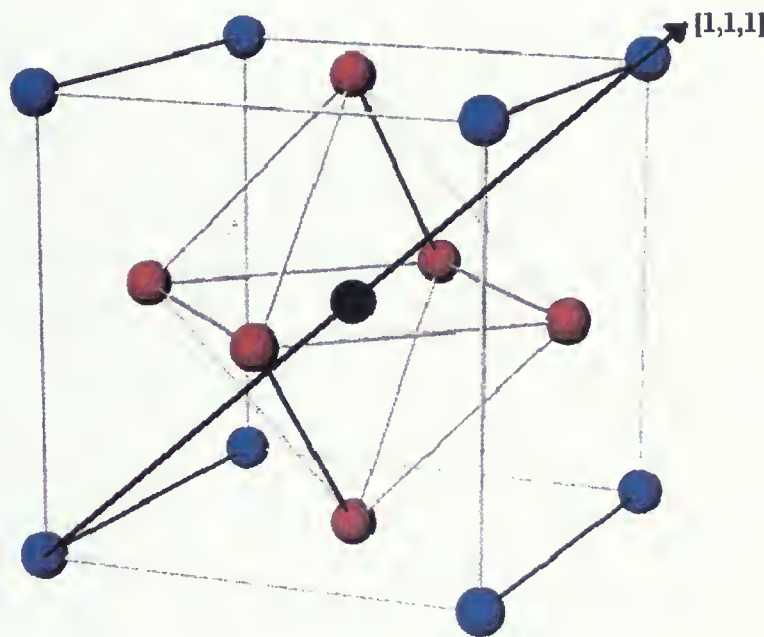


Figure 1.1: Cartoon depiction of the SrTiO_3 Cubic-Perovskite structure. Titanium = Black, Strontium = Blue, and Oxygen = Red.

transition occurs. During this transition, the oxygen octahedron has been found to rotate about the $[1, 1, 1]$ axis of the cubic unit cell. A plot showing measurements of the rotation angle, ϕ , versus temperature is shown in Figure 1.2. Since the bulk material is a continuous array of this repeated structure, it should be kept in mind that adjacent tetrahedrons will rotate in opposite directions

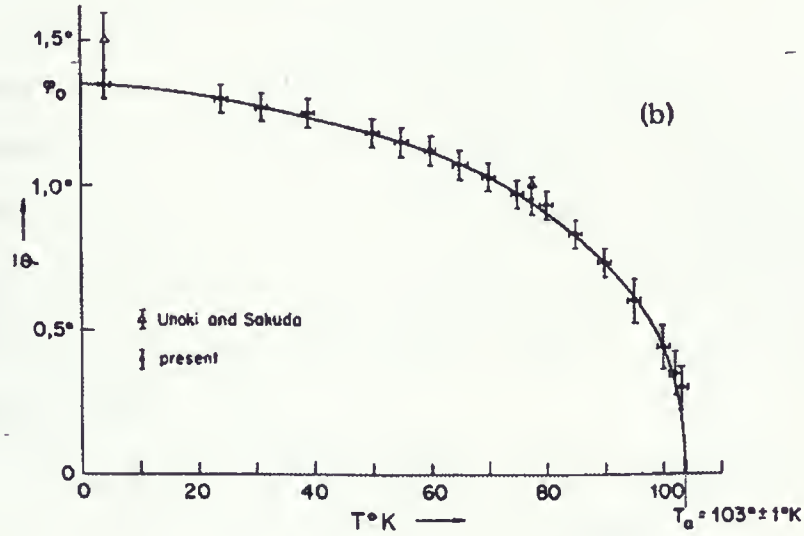


Figure 1.2: Plot showing the angle of rotation, $\bar{\varphi}$, of the oxygen octahedron in SrTiO_3 [1]

[1].

SrTiO_3 is an incipient ferroelectric, meaning it is a material that almost, but not quite, shows a ferroelectric (FE) phase transition. Typical ferroelectrics exhibit two distinct states. Below the transition temperature, T_c , there is a spontaneous polarization, \mathbf{P} , or a net electric dipole moment, \mathbf{p} , per unit volume, V . Above the transition temperature, T_c , there is no spontaneous polarization. Instead, in linear ferroelectrics (such as SrTiO_3):

$$\mathbf{P} = \chi_e \mathbf{E},$$

where \mathbf{E} is the applied electric field, and the dielectric susceptibility, χ_e , exhibits the following Curie-Weiss temperature dependence:

$$\chi_e = \frac{C}{(T - T_c)}.$$

The behaviour of \mathbf{P} in a ferroelectric is analogous to the behaviour of the magnetization, \mathbf{M} , in a ferromagnet. This phenomenon is eloquently summarized by Blinc and Žekš when they write that the ferroelectric phase transition “[represents] a special class of structural phase changes where the

transition from the high to the low symmetry phase is accompanied by the appearance of a spontaneous polarization [2].” Figure 1.3 illustrates that SrTiO_3 exhibits Curie-Weiss behaviour above T_c . Unlike a true ferroelectric material however, SrTiO_3 fails to achieve spontaneous polarization below T_c . The dielectric constant, ϵ , ($\epsilon = \epsilon_0(1 + \chi_e)$) of a ferroelectric will typically diverge as the temperature approaches T_c (105 K). In addition, there exists a net polarization in the absence of an external electric field below this temperature. As shown in Figure 1.4, the divergence of ϵ is clearly not seen in the case of SrTiO_3 .

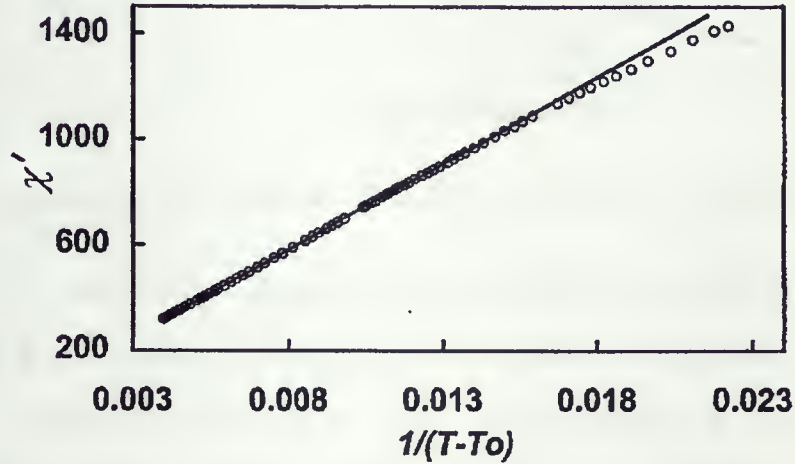


Figure 1.3: Plot showing the temperature dependence of the dielectric susceptibility [3]

During the structural phase transition, a typical ferroelectric crystal splits into many smaller ferroelectric domains (a behaviour again similar to ferromagnets) [4]. If one considers the symmetry of a cubic-perovskite crystal, it is clearly seen that any dipole between the atoms of the cube and octahedron is cancelled in all directions. During the rotation of the tetrahedra, this symmetry would be broken allowing for a net dipole moment to occur if SrTiO_3 were a ferroelectric. The sizes of the domains could then change due to an applied field, allowing for a net polarization in a given direction.

The intrinsic properties of SrTiO_3 have been studied vigorously over the past four decades. The information about its optical properties has been of special interest due to its increased use as a substrate for other semi-transparent materials [6]. Of particular interest in the far-infrared region is the so called “soft” phonon mode which always accompanies a ferroelectric transition [7]. A soft

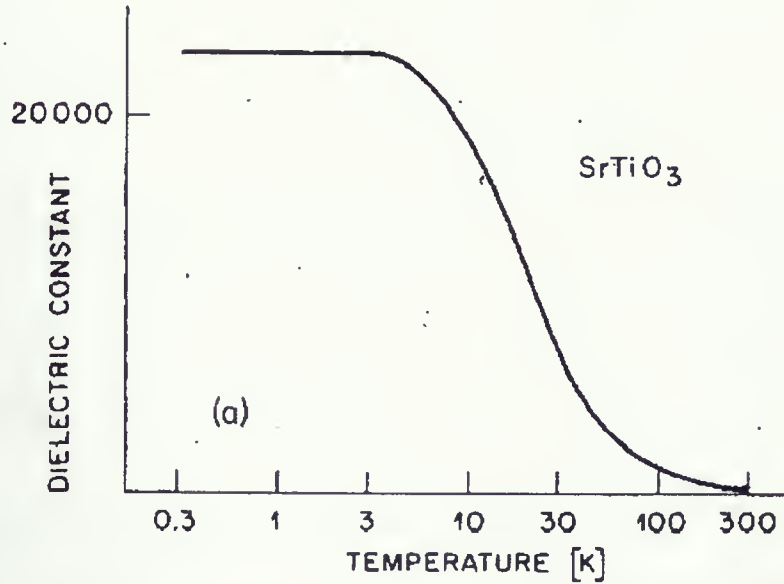


Figure 1.4: Plot showing the low temperature behaviour of the dielectric constant in SrTiO_3 [5]

mode is one where the phonon frequency approaches zero. While the theory of soft-mode behaviour will be discussed in a later section, it should be noted that the soft mode makes the reflectance highly temperature dependent. This, coupled with the cubic-tetragonal structural phase change, which causes changes in the reflectance spectrum, will allow for a thorough test of the system's ability to perform measurements over a range of temperatures.

Though not the subject of this paper, SrTiO_3 can fill a wide variety of roles. As more research is being performed, many new possibilities are arising. For example, SrTiO_3 becomes superconducting at 0.3 K in highly reduced samples with a carrier concentration of roughly 10^{20} cm^{-3} [8] [9].

Chapter 2

Experimental Design

2.1 Overview

Light was reflected off a sample to measure the intensity of the reflected light as a function of its frequency $I_{\text{sample}}(\omega)$. In addition, $I_{\text{reference}}(\omega)$ was measured for an independent reference path. The ratio of the intensity of light from the sample over the reference path was taken (these are called intermediate ratios). After this was repeated several times at different temperatures, gold was evaporated on the sample. Similarly the ratios of the gold coated sample to reference path intensity were taken at corresponding temperatures. Table 2.1 is provided as clarification for this procedure. The motivation for this is explained in depth in the Theory section. For now however, it

Initial Data	$I_{\text{sample}}(\omega)$	$I_{\text{reference}}(\omega)$	$I_{\text{gold-coated sample}}(\omega)$	$I_{\text{reference}}(\omega)$
Intermediate Ratios	$\frac{I_{\text{sample}}(\omega)}{I_{\text{reference}}(\omega)}$		$\frac{I_{\text{gold-coated sample}}(\omega)}{I_{\text{reference}}(\omega)}$	
Reflectance	$\frac{\frac{I_{\text{sample}}(\omega)}{I_{\text{reference}}(\omega)}}{\frac{I_{\text{gold-coated sample}}(\omega)}{I_{\text{reference}}(\omega)}} \times R_{\text{gold}}(\omega)$			

Table 2.1: Process followed to obtain reflectance from collected data

is enough to state that when the ratio of the no-gold intermediate ratio to gold-coated intermediate ratio is calculated, a measure of reflectance $R(\omega)$ is obtained, where:

$$R = \frac{E_r^* E_r}{E_i^* E_i},$$

and E_r and E_i are the reflected and incident electric fields.

While it would seem natural to make use of a monochromatic light source, it is highly impractical. A successful (and easier) method in use is that of Fourier-Transform Infrared (FTIR) Spectroscopy.

While the theory will be explained in a later chapter, the premise is that a measure of light intensity versus frequency is obtained from a measure of light intensity versus path-difference between the mirrors in an interferometer.

A general overview of the components comprising the system is shown in Figure 2.1. As tested,

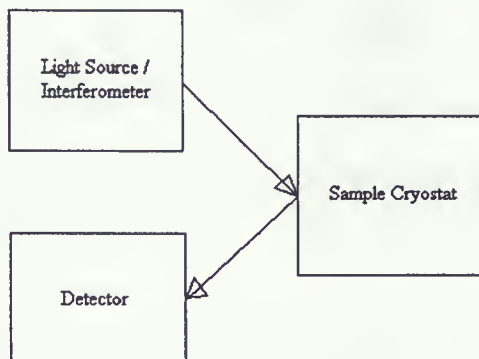


Figure 2.1: Overview of the Experimental Components

the designed apparatus had the capability to perform reflectance measurements on a sample over the range of 4.2 K to 325 K , with an in-situ gold evaporator, self-contained reference path, and a sample chamber pressure of roughly 10^{-8} Torr. In the future, it is anticipated that spectra ranging from the Far-Infrared (FIR) region through to Ultraviolet (UV) will be obtainable.

2.2 Optics

Light was supplied for this experiment by a Brüker IFS 66v/S spectrometer modified for reflectance measurements. A simplified overhead view of the spectrometer, showing the primary components and the factory set light path are shown in Figure 2.2. The Brüker functions as a Michelson interferometer, the theory of which will be discussed Chapter 3. For now it is sufficient to say that with it, intensity versus frequency data may be obtained.

Through the use of different light sources, beamsplitters, detectors, and windows, different

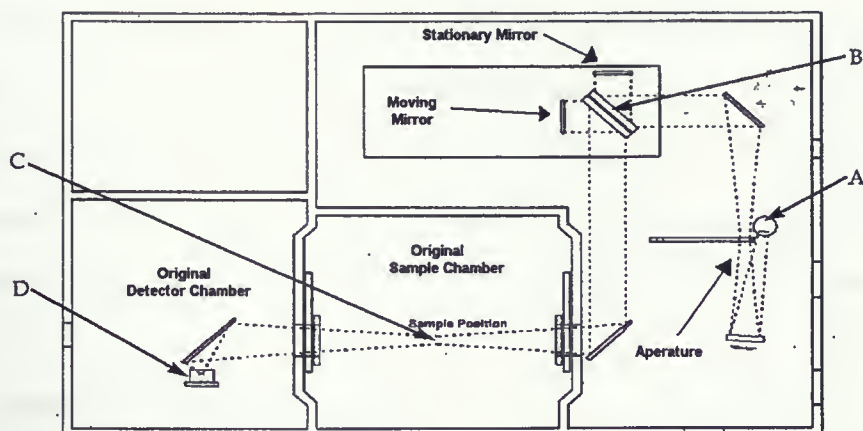


Figure 2.2: Overhead view of the factory configured Brüker spectrometer. A - Light source, B - Beamsplitter, C - Sample position, D - Detector. The factory set light path is shown with a dashed line [10]

frequency ranges may be measured. For the measurements taken during this initial calibration, a Germanium coated $6\ \mu\text{m}$ Mylar beamsplitter was used in conjunction with a Mercury arc lamp, a polypropylene window, and a Diamond/Silicon bolometer (sensitive in the frequency range used for measurement). Utilizing this arrangement, measurements could successfully be reproduced in the $60 - 670\ \text{cm}^{-1}$ range. Table 2.2 illustrates the full potential of this system pending a relatively small quantity of future work.

Component	Type	Working range (cm^{-1})
Beamsplitter	50 μm Mylar	10 – 55
	6 μm Mylar with Ge	60 – 650
	Ge on KBr	370 – 7,500
	Quartz, UV/Vis	4,000 – 52,000
Light Source	Hg Lamp (FIR)	4 – 700
	Globar (Mid-IR)	30 – 7,500
	NIR/VIS Tungsten Lamp	4,000 – 30,000
	Deuterium Lamp (UV)	18,000 – 55,000
Detector	(4.2 K) Bolometer	50 – 700
	MCT	450 – 5,000
	Photo-multiplier	20,000 – 55,000
	Si Photo-diodes	11,000 – 55,000
Windows	Polypropylene	30 – 700
	CaF	1,200 – 55,000

Table 2.2: Frequency ranges of the different optical components [10] [11]

In addition to housing the optical equipment, the Brüker provided a suitable environment for optical measurements. The inside walls were painted black so as to reduce reflections, and the chambers were pumped to remove light absorbing gases. In the far infrared region, both CO₂ and H₂O are known to contribute strong absorption peaks in transmission spectra [10]. For this reason, an internal pressure of roughly 3 mbar (2 Torr) was maintained during the experiment.

2.2.1 The Optical Table

In order to redirect the light from the spectrometer in a desired way, a removeable optical table was placed in the Sample Chamber of the Brüker. In typical arrangements, both the sample and a reference mirror are mounted in the same position, requiring the sample and reference to be interchanged. Since the sample and reference are under vacuum, this would require a sliding O-ring seal which would preclude the achievement of UHV pressures. Hence, in this new configuration a separate internal reference path was used.

Light entering the sample chamber of the Brüker was met by a plane mirror mounted on a swivel base. The rotation of the mirror was driven by a stepper motor, controlled by a user interface outside of the Brüker. This allowed for the choice of light paths at the push of a button. Figure 2.3 illustrates the components of the optical table, and the two distinct light paths. Apertures were placed on each of the light paths in order to control the relative intensity reaching the detector.

Underneath the optical table, an optical gate detects the absolute orientation of the moving mirror. The controller then relates this to its user-set positions, ensuring that steps are never “lost.” After initial testing, it was noted that the endpoint positions were not being reproduced with a high enough degree of accuracy. This led to the addition of adjustable mechanical stops placed at each of the endpoints. In the present configuration, the stepper motor is designed to drive to one step beyond the mechanical stops. This has been found to essentially remove any error associated with the mirror’s position. A serial port was added to the initial design of the controller. This could allow for a computer to control the position of the mirror, removing the need for human intervention after each scan.

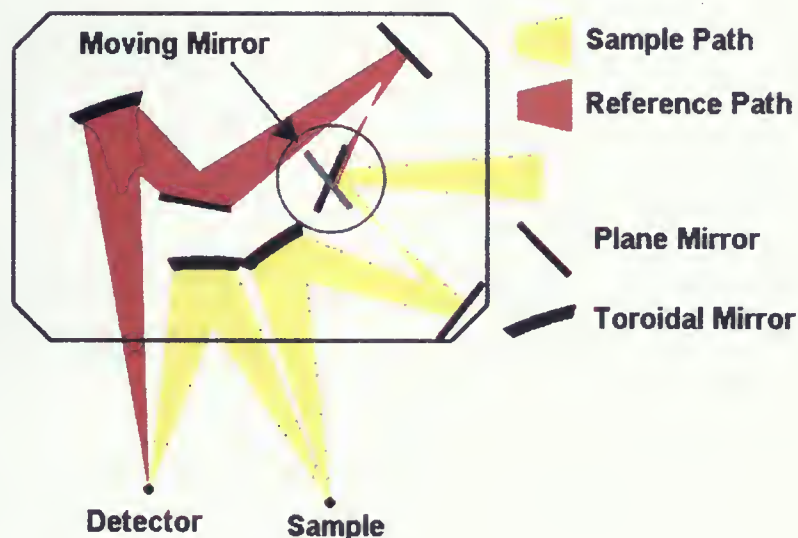


Figure 2.3: General layout of the optical table, depicting the individual light paths

2.3 Sample Chamber

The primary functions of the sample chamber are to provide rigid support for the sample, a suitable environment for optical experiments, and a means of depositing gold without disturbing the position of the sample.

As mentioned, gases exist in the air which can absorb light and lead to a decrease in light intensity reaching the sample, and subsequently the detector. To combat the unwanted condensation of ice, a sample chamber was designed which incorporated the use of ultra-high vacuum (UHV) flanges. A turbopump was permanently mounted as close as possible to the sample, providing the system with a lowest recorded pressure of roughly 4×10^{-8} Torr. It is believed that allowing the sample chamber to cool after purposefully heating it, a process commonly known as “baking,” will allow for even lower pressures to be achieved.

The sample itself was mounted within a cryostat which was fixed to the spectrometer through the use of the wedge shaped adapter shown in Figure 2.4. The adapter was chosen to be shaped as a wedge in order to accommodate the existing light cone exiting the spectrometer. Contained within the adapter is a window which acts to isolate the sample chamber from the spectrometer. The

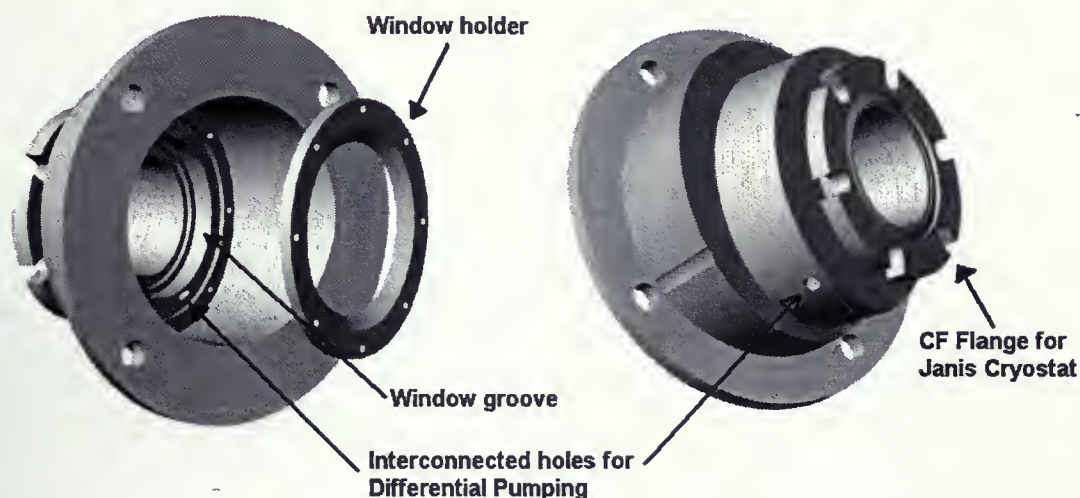


Figure 2.4: Wedge-shaped sample cryostat adapter with differential pumping unit

presence of a window poses a challenge to achieving UHV pressures in the sample chamber. Common rubber O-Rings act as a seal between the wedge/spectrometer and wedge/window interfaces, and cannot sustain a large pressure gradient. Hence a “differential pumping” section was incorporated into the design of the wedge. This allows for the space surrounding the window to be pumped out with an intermediate pressure of roughly 7×10^{-3} Torr. A cross-section of the primary components of such a system are shown in Figure 2.5. The low, intermediate, and ultra-high vacuum regions labelled in the diagram correspond to Brüker Spectrometer, roughing line, and sample chamber.

One of the reasons for requiring such a low pressure within the sample chamber is to ensure that a high quality gold layer can be deposited on the sample. At the appropriate time, a flap swings between the adapter wedge and the sample cryostat to protect the window against gold particles. This process is illustrated in Figure 2.6. Mounted on the sample side of the flap is a tungsten filament, wrapped with gold loops. Current is passed through the filament, causing it to heat-up beyond the melting point of gold. In the present configuration, the filament has a typical resistance of $0.6 \, \Omega$. A current of 1 A is applied for 10 s, followed immediately by a current of 2 A for 30 s. After a short wait, the flap is opened and the experiment is continued. Following an experiment, the gold film can be easily removed from the sample allowing for repeated use of the same sample.

The sample itself is mounted on a cone shaped mount, fitted to the cold-finger of a Janis In-

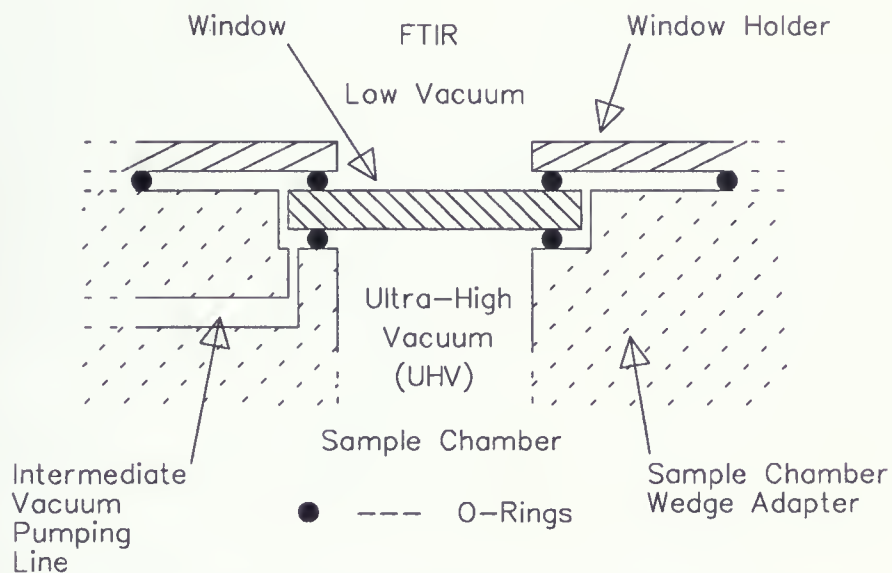


Figure 2.5: A cross-sectional view of the Sample Wedge's differential pumping unit, showing the three pressure zones. The low vacuum zone may be at atmospheric pressure during sample alignment.

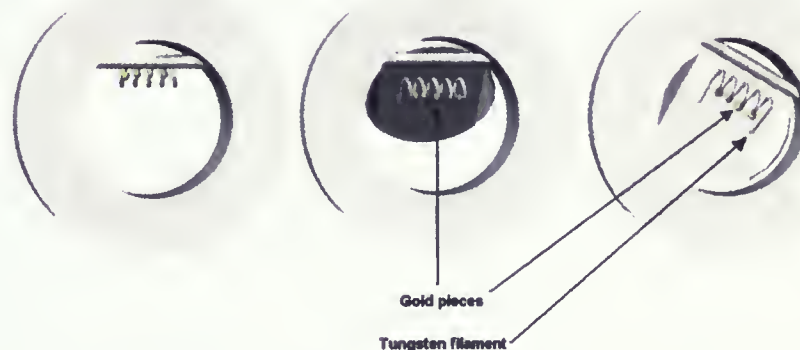


Figure 2.6: Cartoon depiction of the gold evaporator unit swinging from open (left) to closed (right), in preparation for an evaporation.

dustries ST-400 continuous-flow cryostat. Sample cooling was performed by circulating a cryogenic liquid (nitrogen or helium) through a chamber in thermal contact with the cold finger. A 50 Ω heating element was attached to the cold-finger allowing for temperature control and higher temperatures to be achieved. The power supplied to the heating element was controlled by a supplied Cryocon 32 temperature controller which utilized a temperature sensor (Si-diode) located within the cryostat, above the cold finger. Through careful adjustment of the cryogen flow rate, a wide range of temperatures could be easily maintained without loss due to boil-off.

2.4 Detector

The reflected light from either the reference mirrors or the sample eventually strikes the bolometer. The bolometer's output voltage is proportional to the intensity of light which strikes it in the following way [12]. A bismuth coated diamond substrate absorbs the incident radiation, causing it to change temperature. A substrate with a low heat capacity is desired so that minute changes in absorbed radiation are detectable. These changes in temperature are then detected by a doped semiconductor (namely silicon) whose resistivity is extremely sensitive to temperature. A current passing through the semiconductor is used to measure the resistivity changes. Figure 2.7 shows the elements used in construction of a typical bolometer. Due to differing bolometer constructions consideration must be taken to ensure that the bolometer used is sensitive to the frequency range of interest. In order to capture the behaviour of SrTiO_3 at extremely low frequencies, a bolometer designed to work at 4.2 K was used due to its high sensitivity in the frequency range of 50 cm^{-1} to 700 cm^{-1} .

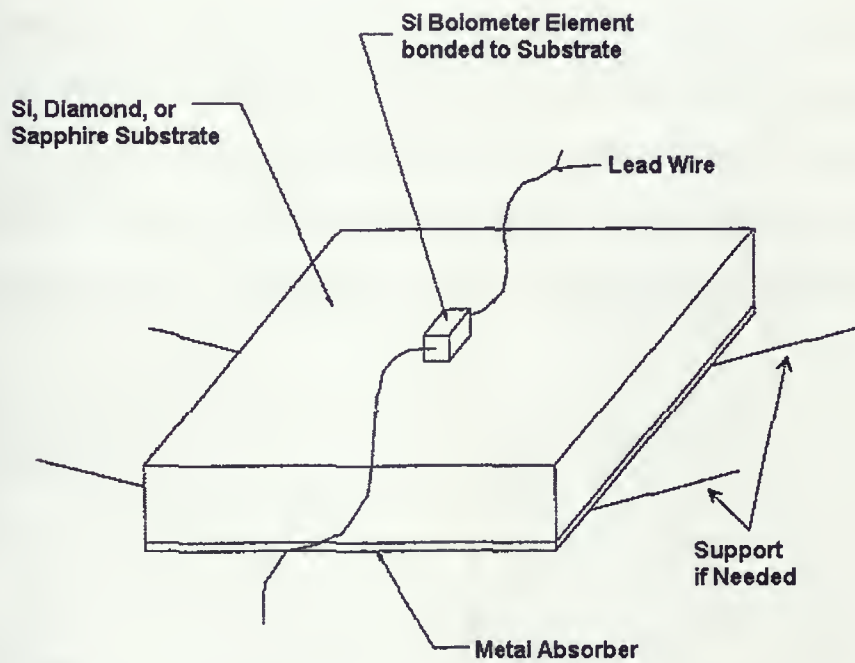


Figure 2.7: Schematic of a typical Bolometer. (Light is incident on the metal absorber side) [13].

Chapter 3

Theory

3.1 Overview

As mentioned in the previous section, the raw data gathered throughout the experiment is a collection of intensity readings at varying path differences for the light passing through the Michelson interferometer in the Bruker. Through the use of Fourier-Transformations these Interferograms (Intensity, I , versus Path Difference, x) were turned into Power Spectra (Intensity versus Frequency, ω). Typical examples of both an Interferogram and Power Spectrum are shown in Figure 3.1.

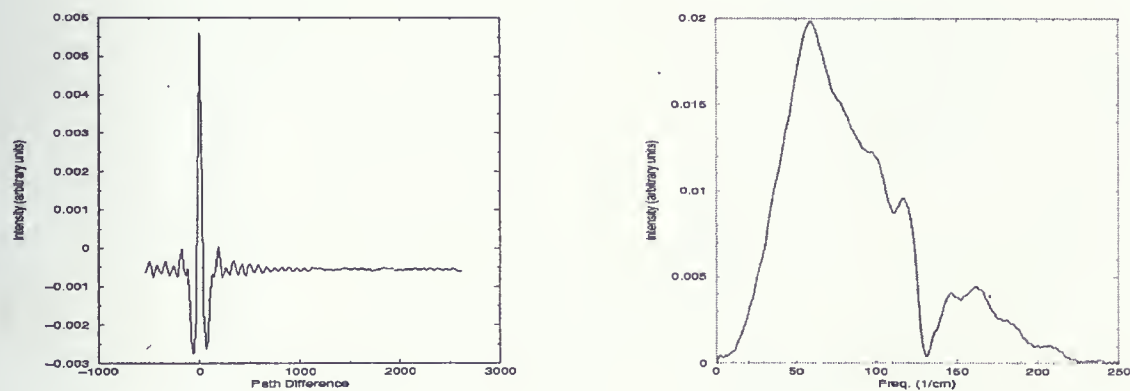


Figure 3.1: A typical Interferogram and its Fourier-Transformed Power Spectrum

After each set of Power Spectra were collected for both the sample and reference mirror a ratio of the two was taken. Averages of many of these “Intermediate Ratios” were taken at specific temperatures both for a bare and gold-coated sample. The ratio of the sample’s average Intermediate Ratio over the gold-coated sample’s average Intermediate Ratio was found. This spectrum is then

multiplied by the known reflectance of gold, R_{gold} . As discussed later in this section, the result is referred to as the “Absolute Reflectance”. All of the preceding calculations were performed by a computer using software designed specifically for this task. The theory and motivation behind these calculations will be presented in the following sections.

3.2 Fourier-Transform Spectroscopy

The explanation of the Fourier-Transform process is outlined below, and closely follows the works of Möller and Rothschild [14] and Bell [15]. Figure 3.2 [14] shows a layout for a Michelson Interferometer, which will be used in describing the theory. The derivations provided for the Michelson

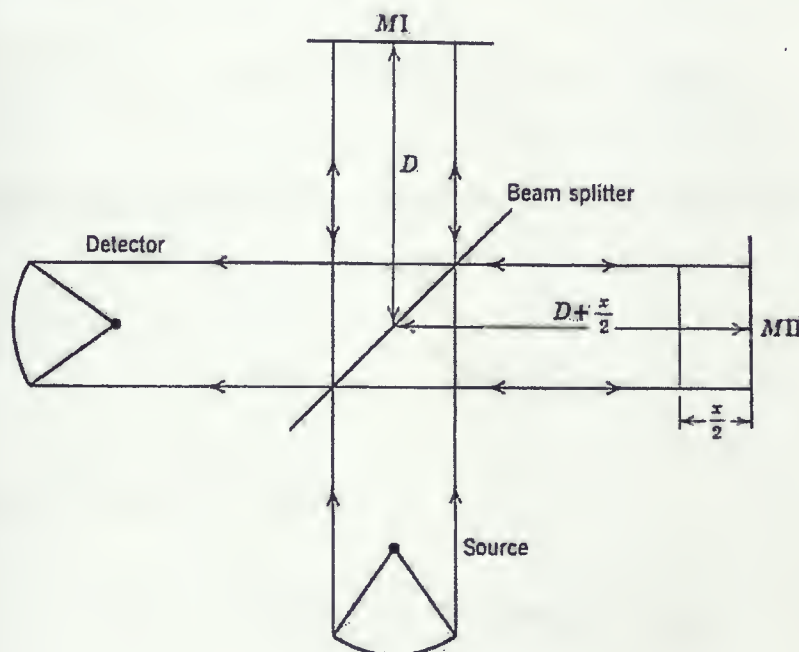


Figure 3.2: Schematic of a Michelson Interferometer [14]

Interferometer will hold true for the Bruker. Notice in Figure 3.2, one mirror is displaced a distance of $\frac{x}{2}$ further from the beam splitter than the other. First consider monochromatic light of frequency ω_0 as a light source. When light from the two split paths recombine at the beam splitter, they will

do so with an intensity of:

$$\begin{aligned}
 I(x) &= 4S \cos^2(\pi\omega_0 x) \\
 &= 2S(1 + \cos(2\pi\omega_0 x)) \\
 &= 2S + 2S \cos(2\pi\omega_0 x),
 \end{aligned} \tag{3.1}$$

where S is defined as the amplitude of each recombining beam squared (assuming that the beam-splitter splits the beam equally).

S is now turned into a function of ω in order to account for a polychromatic light source (as is the case with the Bruker). Adding all the frequency components in Equation 3.1 produces:

$$I(x) = \int_0^\infty 2S(\omega) d\omega + \int_0^\infty 2S(\omega) \cos(2\pi\omega x) d\omega. \tag{3.2}$$

If we were to consider a position of the mirrors where $x = 0$ (called the “zero-path”) we see that:

$$I(0) = 2 \int_0^\infty 2S(\omega) d\omega.$$

Substituting this into Equation 3.2 yields:

$$\begin{aligned}
 I(x) &= \frac{1}{2}I(0) + \int_0^\infty 2S(\omega) \cos(2\pi\omega x) d\omega \\
 &= \frac{1}{2}I(0) + s(x),
 \end{aligned}$$

where $s(x)$ is called the “interferogram function”.

Figure 3.3 illustrates a typical relationship between the values described above [14]. Note however that in Figure 3.3 the values of $I(0)$ and $I(x)$ are labelled as $g(0)$ and $g(x)$. It is this interfer-

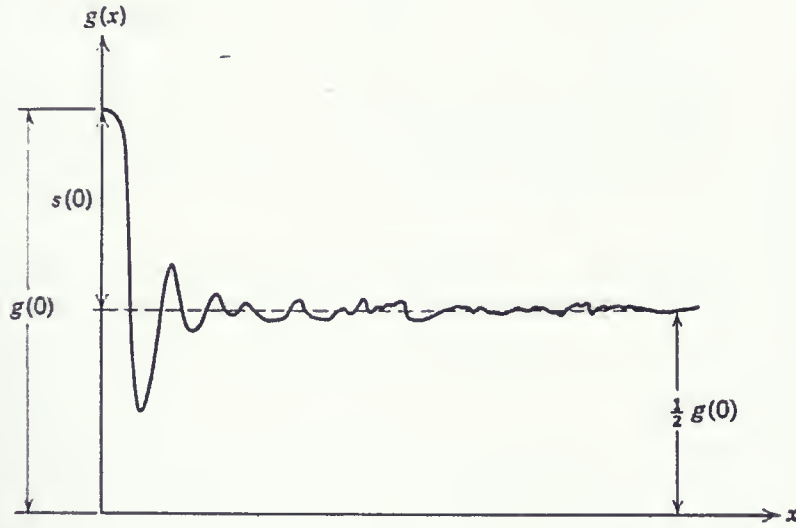


Figure 3.3: Typical relationship between $I(x)$ (labelled $g(x)$) and $s(x)$ [14]

ogram function which leads to the desired $S(\omega)$ given the following Fourier Transform pair:

$$\begin{aligned}
 s(x) &= g(x) - \frac{1}{2}g(0) \\
 &= \int_{-\infty}^{+\infty} S(\omega) \cos(2\pi\omega x) d\omega \\
 S(\omega) &= \int_{-\infty}^{+\infty} s(x) \cos(2\pi\omega x) dx
 \end{aligned}$$

In actuality, the calculation of the integrals does not extend from a path difference of $-\infty$ to $+\infty$. Usually multiplication by a weighted window function is used:

$$S(\omega) = \int_{-\infty}^{+\infty} w(x) s(x) \cos(2\pi\omega x) dx$$

where,

$$w(x) = \begin{cases} \text{weight func.}, & -L \leq x \leq L; \\ 0, & \text{elsewhere.} \end{cases}$$

The weight function may take any form such as 1 , $1 - \left|\frac{x}{L}\right|$, or $\left(1 - \frac{x^2}{L^2}\right)^2$ [14].

3.2.1 Optical Constants of Solids

As a starting point for this discussion, it is useful to point out the difference between the complex reflection coefficient r , which relates the incident, E_{inc} , and reflected, E_{ref} , electric fields with [16]:

$$\begin{aligned} E_{\text{ref}} &= r E_{\text{inc}} \\ &= \rho e^{i\theta} E_{\text{inc}}, \end{aligned}$$

and the measured quantity of reflectance R which is actually $r^* r = |r|^2$.

The complex index of refraction $N(\omega) = n(\omega) + ik(\omega)$, is related to both the reflection coefficient and the reflectance in the following way [16]:

$$r(\omega) = \frac{n(\omega) + ik(\omega) - 1}{n(\omega) + ik(\omega) + 1} \quad (3.3)$$

$$R(\omega) = \frac{(n(\omega) - 1)^2 + k(\omega)^2}{(n(\omega) + 1)^2 + k(\omega)^2} \quad (3.4)$$

So then:

$$n(\omega) = \frac{1 - r(\omega)^2}{1 + r(\omega)^2 - 2r(\omega) \cos \Theta(\omega)} \quad (3.5)$$

$$k(\omega) = \frac{2r(\omega) \sin \Theta(\omega)}{1 + r(\omega)^2 - 2r(\omega) \cos \Theta(\omega)} \quad (3.6)$$

The complex index of refraction is related to the complex dielectric function $\epsilon(\omega) = \epsilon_1(\omega) + i\epsilon_2(\omega)$ in the following way [16]:

$$\begin{aligned} \sqrt{\epsilon(\omega)} &\equiv N(\omega) \\ \epsilon(\omega) &= (n(\omega) + ik(\omega))^2. \end{aligned}$$

We may then write:

$$\epsilon_1(\omega) = n(\omega)^2 - k(\omega)^2 \quad (3.7)$$

$$\epsilon_2(\omega) = 2n(\omega)k(\omega). \quad (3.8)$$

The experimentally collected reflectance data is used to find the parameters of a theoretical (complex) $\epsilon(\omega)$. As will be discussed later, this $\epsilon(\omega)$ is referred to as the factorized dielectric function. The fitting process proceeds as follows. Theoretical ϵ_1 and ϵ_2 spectra are created by a computer using some starting parameters in a fitting program (Igor Pro) [17]. These spectra are converted into a complex index of refraction spectrum using the following relations [18]:

$$n = \left\{ \frac{1}{2}[(\epsilon_1^2 + \epsilon_2^2)^{\frac{1}{2}} + \epsilon_1] \right\}^{\frac{1}{2}} \quad (3.9)$$

$$k = \left\{ \frac{1}{2}[(\epsilon_1^2 + \epsilon_2^2)^{\frac{1}{2}} - \epsilon_1] \right\}^{\frac{1}{2}}. \quad (3.10)$$

Through the use of Equation 3.4, a theoretical reflectance spectrum is calculated. This spectrum is compared to the collected data and the parameters are adjusted using the Igor Pro fitting routines until the best fit is obtained.

3.3 Lorentz Model

Models have been developed over the years in order to relate physical quantities to the complex dielectric function (and other response functions). The oldest and simplest of these is the Lorentz model where one assumes that all absorption processes behave as forced-damped harmonic oscillators. In the far-infrared region, a common absorption process would be the coupling of light to transverse optical phonons. The oscillator is a charged ion pair with reduced mass, m , and effective charge, q .

We may write an expression for the the displacement of the positive ions with respect to the

negative ions, \mathbf{r} , within a local electric field \mathbf{E}_{loc} as [18]:

$$m \frac{d^2 \mathbf{r}}{dt^2} + m\Gamma \frac{d\mathbf{r}}{dt} + m\omega_0^2 \mathbf{r} = q\mathbf{E}_{\text{loc}}. \quad (3.11)$$

This expression represents a forced-damped harmonic oscillator. The frequency, ω_0 , found in the restoring term, $m\omega_0^2$, represents the transverse optical phonon frequency. Solutions of this equation at different ω_0 would then model different lattice vibrations (or electronic transitions, where m would be the mass of an electron). The associated damping term in this relationship, $m\Gamma \frac{d\mathbf{r}}{dt}$, accounts for inelastic scattering (energy loss) within the material, where Γ is the energy relaxation rate. If we consider a local electric field, \mathbf{E}_{loc} , and displacement, \mathbf{r} , of the form:

$$\mathbf{E}_{\text{loc}} = \mathbf{E}_0 e^{-i\omega t} \quad (3.12)$$

$$\mathbf{r} = \mathbf{r}_0 e^{-i\omega t}. \quad (3.13)$$

Solving Equation 3.11 then yields:

$$\mathbf{r} = \frac{q\mathbf{E}_{\text{loc}}}{m} \frac{1}{(\omega_0^2 - \omega^2) - i\Gamma\omega}. \quad (3.14)$$

Assuming then that the displacement, \mathbf{r} , is small, the following relationship exists between the dipole moment, \mathbf{p} , ionic polarizability, $\alpha(\omega)$, and local electric field:

$$\mathbf{p} = \alpha(\omega)\mathbf{E}_{\text{loc}}$$

where \mathbf{p} and \mathbf{r} are related to the number of dipoles per unit volume, N , through the following relation:

$$\mathbf{p} = Nq\mathbf{r}.$$

So, the polarizability would be given by:

$$\alpha(\omega) = \frac{Nq^2}{m} \frac{1}{(\omega_0^2 - \omega^2) - i\Gamma\omega}. \quad (3.15)$$

Making the assumption that \mathbf{E}_{loc} equals the macroscopic electric field, \mathbf{E} , a displacement, \mathbf{D} , is defined such that:

$$\begin{aligned} \mathbf{D} &= \epsilon \mathbf{E} \\ &= \mathbf{E} + 4\pi \mathbf{P} \end{aligned}$$

Which after substituting the following two expressions:

$$\begin{aligned} \mathbf{P} &= \chi_e \mathbf{E} \\ \chi_e &= N\alpha, \end{aligned}$$

becomes:

$$\epsilon = 1 + 4\pi N\alpha.$$

Making the substitution for $\alpha(\omega)$ from Equation 3.15:

$$\epsilon(\omega) = 1 + \frac{\omega_p^2}{(\omega_0^2 - \omega^2) - i\Gamma\omega}, \quad (3.16)$$

where ω_p , commonly referred to as the “plasma frequency,” is a parameter related to the strength of coupling of a mode to the incident electro-magnetic radiation, and is given by:

$$\omega_p^2 = \frac{4\pi Nq^2}{m}.$$

Taking the real and imaginary parts of Equation 3.16, we see:

$$\begin{aligned}\epsilon_1(\omega) &= 1 + \frac{\omega_p^2(\omega_0^2 - \omega^2)}{(\omega_0^2 - \omega^2)^2 + \Gamma^2\omega^2} \\ \epsilon_2(\omega) &= \frac{\omega_p^2\Gamma\omega}{(\omega_0^2 - \omega^2)^2 + \Gamma^2\omega^2}\end{aligned}$$

In a real solid, there will be numerous oscillators. Some of these will be electronic, while others will be ionic. If we consider the case where $\omega_0 \gg \omega$ and $\omega_0 \gg \Gamma$ (as is the case of an electronic transition contributing to $\epsilon(\omega)$ in the IR frequency range), it is seen that:

$$\begin{aligned}\epsilon_1 &\cong 1 + \left(\frac{\omega_p}{\omega_0}\right)^2 \equiv \epsilon_\infty \\ \epsilon_2 &\cong 0.\end{aligned}$$

The term ϵ_∞ is used to account for the contributions from all the high-frequency oscillators in $\epsilon_1(\omega)$ for the far infra-red region. In summary, the Lorentz model for the dielectric function in the IR range, accounting for several ionic phonon modes (as well as higher frequency electronic modes) will be given by:

$$\epsilon(\omega) = \epsilon_\infty + \sum_n \frac{\omega_{p_n}^2}{(\omega_{0_n}^2 - \omega^2) - i\Gamma_n\omega}. \quad (3.17)$$

Figure 3.4 illustrates $n(\omega)$, $k(\omega)$, and $R(\omega)$ spectra generated from an $\epsilon(\omega)$ consisting of one Lorentz oscillator, where $\epsilon_\infty = 1$.

3.4 Factorized Dielectric Model

Early research on SrTiO_3 (and other highly ionic insulators) had shown that the classical Lorentz model did not perform an adequate job of representing the data. Rather, a more complex model is needed to fit the data presented by SrTiO_3 [7][19].

In the factorized dielectric function, the transverse-optical (TO) and longitudinal-optical (LO)

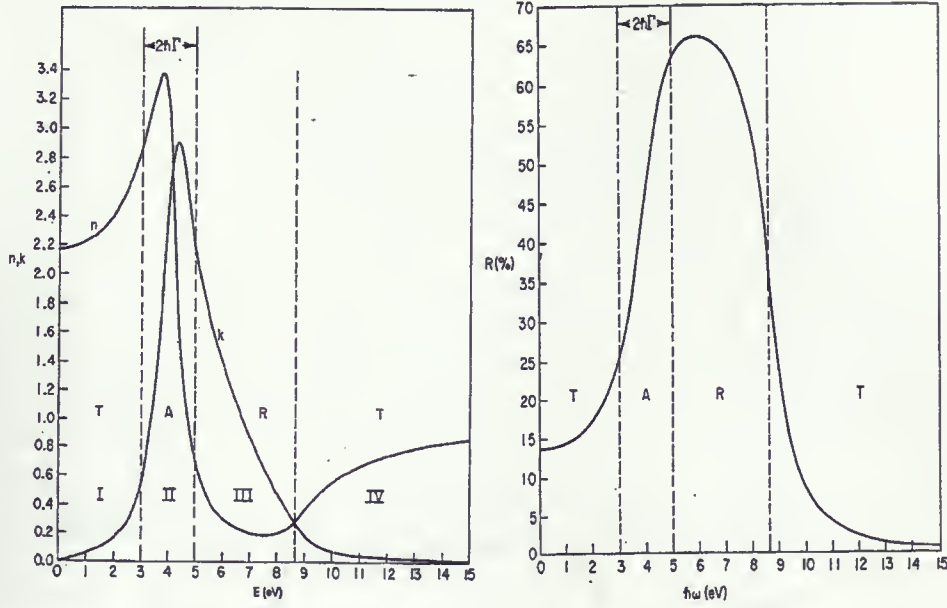


Figure 3.4: Theoretically produced $n(\omega)$ and $k(\omega)$ (left), and $R(\omega)$ (right) for a single Lorentz oscillator centred about 4 eV [18]

phonon modes are permitted to have their own frequencies, Ω , and damping, γ . The following form of the complex dielectric function has been previously shown to be effective in capturing the behaviour of SrTiO_3 [7]:

$$\epsilon(\omega) = \epsilon_\infty \prod_j \frac{\Omega_{jLO}^2 - \omega^2 + i\gamma_{jLO}\omega}{\Omega_{jTO}^2 - \omega^2 + i\gamma_{jTO}\omega}. \quad (3.18)$$

It has been shown that in the case where the longitudinal (γ_{LO}) and transverse (γ_{TO}) scattering rates are equal, the factorized dielectric model reduces to the simple case of the Lorentz model [20].

Figure 3.5 shows a sample of the experimental data with fits to both the Lorentz and Factorized Dielectric models. As can clearly be seen, the Factorized Dielectric model fits the data significantly better than the Lorentz model. This is to be expected as the Factorized Dielectric model has four fitting parameters versus the three found in the Lorentz model.

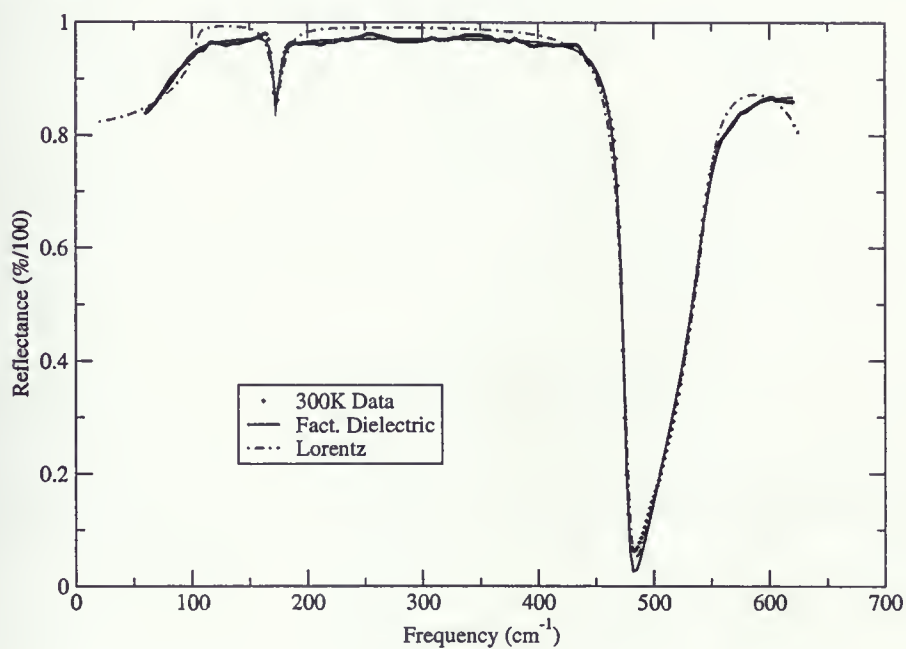


Figure 3.5: Comparison of the ability of the Lorentz and Factorized Dielectric models in capturing the structure of the 300 K data

3.5 Lyddane-Sachs-Teller (LST) Relationship

The association of a soft mode with the ferroelectric transition can be seen in the Lyddane-Sachs-Teller (LST) relation, which is explained as follows. Consider the dielectric function of a single oscillator without damping [16]:

$$\epsilon(\omega) = \epsilon_{\infty} + \frac{4\pi Nq^2}{m} \frac{1}{(\omega_{TO}^2 - \omega^2)}. \quad (3.19)$$

Which, through the use of the following relationships [21]:

$$\begin{aligned} \omega_p^2 &= \frac{4\pi Ne^2}{m} \\ &= \epsilon_{\infty} (\omega_{LO}^2 - \omega_{TO}^2), \end{aligned} \quad (3.20)$$

becomes:

$$\epsilon(\omega) = \epsilon_{\infty} \left(\frac{\omega_{LO}^2 - \omega^2}{\omega_{TO}^2 - \omega^2} \right). \quad (3.21)$$

Setting $\omega = 0$ in this expression gives rise to the famous Lyddane-Sachs-Teller relation for a single oscillator:

$$\frac{\epsilon_0}{\epsilon_{\infty}} = \frac{\omega_{LO}^2}{\omega_{TO}^2}. \quad (3.22)$$

Verification of the LST relation is performed by comparing neutron scattering data and infrared reflectance data from the same sample. Values of ϵ_{∞} and ϵ_0 can be obtained directly from the reflectance data as follows. Since at extremely low or high frequencies k is essentially zero, the reflectance is approximated by:

$$R \cong \left(\frac{n-1}{n+1} \right)^2.$$

Through the substitution of Equation 3.7 this would indicate that:

$$R(\omega \rightarrow 0) \cong \left(\frac{\sqrt{\epsilon_0} - 1}{\sqrt{\epsilon_0} + 1} \right)^2,$$

$$R(\omega \gg \text{IR}) \cong \left(\frac{\sqrt{\epsilon_\infty} - 1}{\sqrt{\epsilon_\infty} + 1} \right)^2.$$

Alternatively, ϵ_0 can be determined through capacitance measurements. The values of ω_{LO} and ω_{TO} can be accurately found using neutron scattering data (at $\mathbf{k} = 0$). Figure 3.6 provides ω versus \mathbf{k} for both Ge and KBr. As shown, the tranverse and longitudinal branches are the same for Ge at

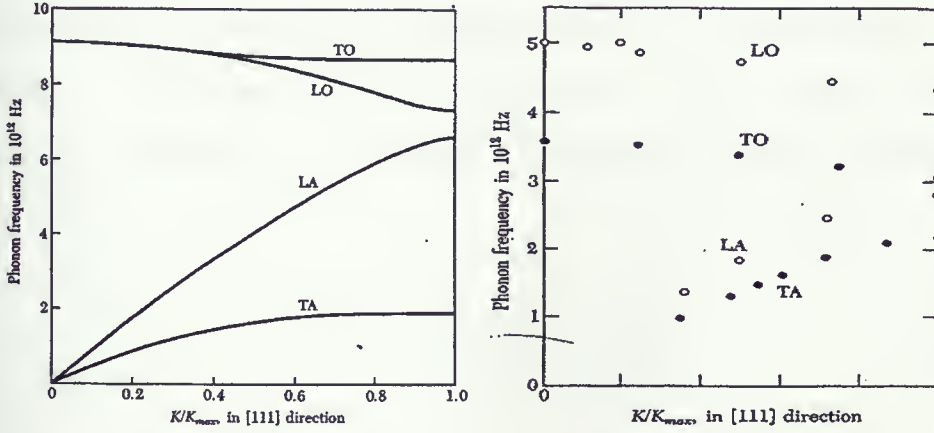


Figure 3.6: Plots showing ω_{LO} and ω_{TO} versus \mathbf{k} for both Ge (left) and KBr (right) measured using neutron scattering [16]

$\mathbf{k} = 0$. This would indicate that:

$$\frac{\omega_{LO_{Ge}}^2}{\omega_{TO_{Ge}}^2} \cong 1 \quad (3.23)$$

and:

$$\frac{\omega_{LO_{KBr}}^2}{\omega_{TO_{KBr}}^2} \cong \left(\frac{5}{3.6} \right)^2$$

$$\cong 1.93 \quad (3.24)$$

Comparing these directly to measurements presented by Kittel (Chapter 10) [16], we see:

$$\begin{aligned}\frac{\epsilon_{0_{Ge}}}{\epsilon_{\infty_{Ge}}} &= \frac{15.8}{15.8} \\ &= 1\end{aligned}\tag{3.25}$$

and:

$$\frac{\epsilon_{0_{KBr}}}{\epsilon_{\infty_{KBr}}} \cong 1.90\tag{3.26}$$

This is direct evidence from a variety of sources indicating the accuracy of the LST relation. Furthermore, Equation 3.22 suggests that if a TO mode softens ($\omega_{TO} \rightarrow 0$) then ϵ_0 will increase (as shown in Figure 1.4). An adaptation of the LST relationship proposed by Barker for use with SrTiO_3 is given by [22]:

$$\frac{\epsilon_0(T)}{\epsilon_\infty} = \frac{\Omega_{1LO}^2}{\Omega_{1TO}^2} \frac{\Omega_{2LO}^2}{\Omega_{2TO}^2} \frac{\Omega_{3LO}^2}{\Omega_{3TO}^2},$$

where Ω_1 , Ω_2 and Ω_3 are the frequencies of the three phonon modes.

3.6 Soft-Mode Behaviour

One of the striking discoveries surrounding the optical properties of SrTiO_3 is the presence of a “soft” transverse optical phonon mode. The term “soft” in this case refers to the fact that the frequency of the lowest phonon-mode decreases. Plots of the soft-mode frequency, Ω_s (Ω_{1TO}), have yielded a behaviour of the form [7]:

$$\Omega_s^2 = A(T - T_c),\tag{3.27}$$

where A is a constant, for all temperatures above 50 K as shown in Figure 3.7. This relationship is a direct result of the LST relationship combined with the $\frac{1}{T-T_c}$ temperature dependence of the

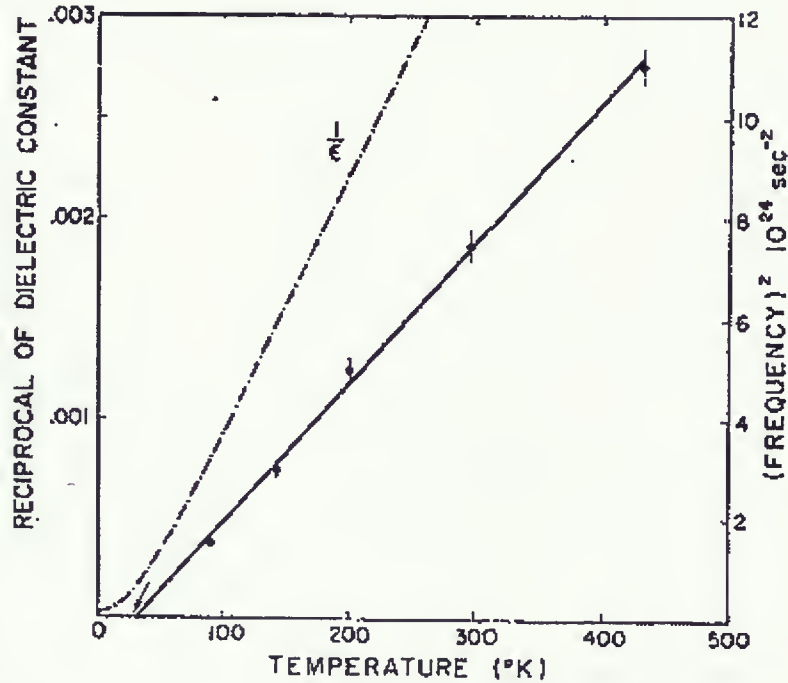


Figure 3.7: Previous measurements of the temperature dependence of the “soft” phonon mode (solid line) [4].

dielectric constant, ϵ , shown in Figure 1.3.

Further studies have shown a strong dependence of the soft-mode frequency on the presence and strength of an applied electric field. Although this phenomenon was not studied, as the apparatus is not designed with this purpose in mind, plots of the soft-mode frequency versus applied field are shown in Figure 3.8 for interest sake [23]. As shown, the interaction of the soft-mode and the applied external field is highly temperature dependent.

3.7 SrTiO₃ Lattice Dynamics

In a group-theory study of the properties of La_{1-x}Sr_xFeO₃ and La_{1-x}Sr_xCoO₃ (ABO₃ perovskites similar in nature to SrTiO₃), the four triply degenerate ($\mathbf{k} = 0$) vibrational modes of the lattice were proposed [24], which are shown in Figure 3.9. Of these, the infrared-active ones are the stretching, bending, and external modes. As suggested by Cowley, through fitting data from neutron spectroscopy data to various models, the lowest frequency (soft-phonon) mode was associated with

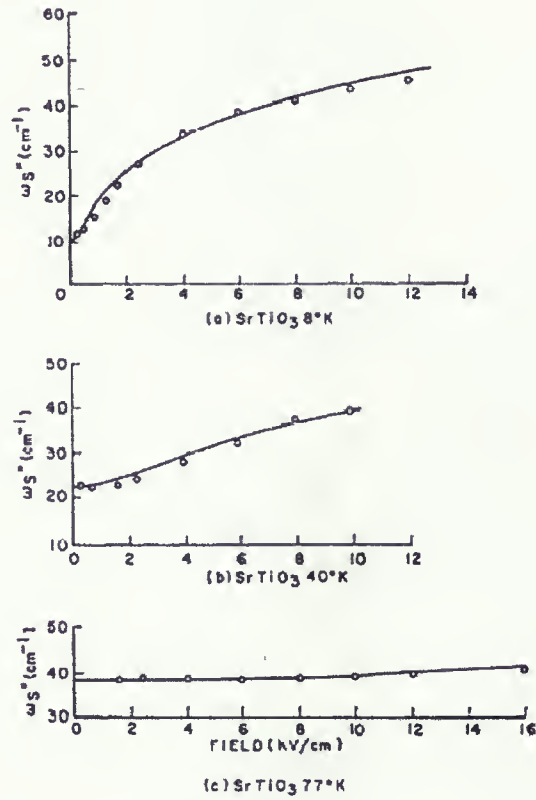


Figure 3.8: Plots of the soft-mode frequency versus applied electric field at 8 K (top), 40 K (middle), and 77 K (bottom).

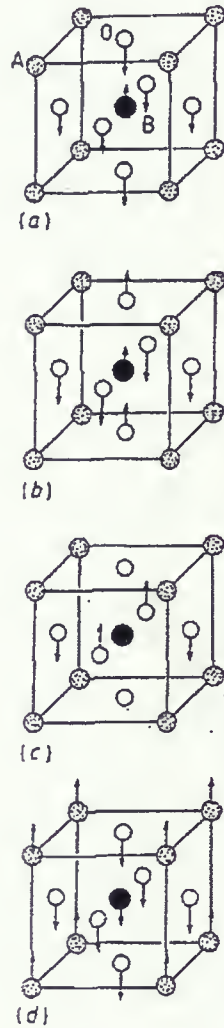


Figure 3.9: Depictions of the stretching, bending, inactive, and external vibrational modes for a SrTiO_3 crystal. [24]

the stretching mode [4]. It was shown that this was primarily a movement of the titanium atom against the remainder of the lattice [4].

The cubic-tetragonal structural transition ($T_c = 110$ K) has a dramatic effect on the lattice dynamics. Each triply degenerate mode splits into doubly degenerate and singly degenerate modes.

Chapter 4

Measurements

The main reason for choosing SrTiO_3 to test the effectiveness of the newly developed system was the large number of previous studies. It was expected that there would not be any “surprises,” and that any deviations from historical research would indicate difficulties with the setup. Though not accounting for any great differences, it should be noted that light was incident along the c-axis of the single crystal cubic/tetragonal Perovskite samples, while this was not necessarily the case with some of the other research.

4.1 Previous Reflectance Measurements

Although the reflectance of SrTiO_3 has been measured many times in the past, modern advances in technology have led to results containing a much higher degree of resolution. As a result, structure which had previously been overlooked has only been observed in the most recent of publications. For this reason, the calibration of the new apparatus will be compared with the work of Petzelt et al [25] and Servoin et al [7]. Figure 4.1 shows previous reflectance measurements of powder samples from 10 K to 300 K [25] and of a single crystal from 300 K to 1200 K [7].

4.2 New Reflectance Measurements

Approximately 400 scans were taken for each of the intermediate ratios over the course of two days for the 10 K, 150 K, and 300 K data. It is of particular interest to note the order of the measurements, as an unresolved issue has been raised as a result. Subsequently, further measurements were made on the same sample at 90 K, 125 K, 225 K, and 300 K, in an effort to capture the behaviour of the sample

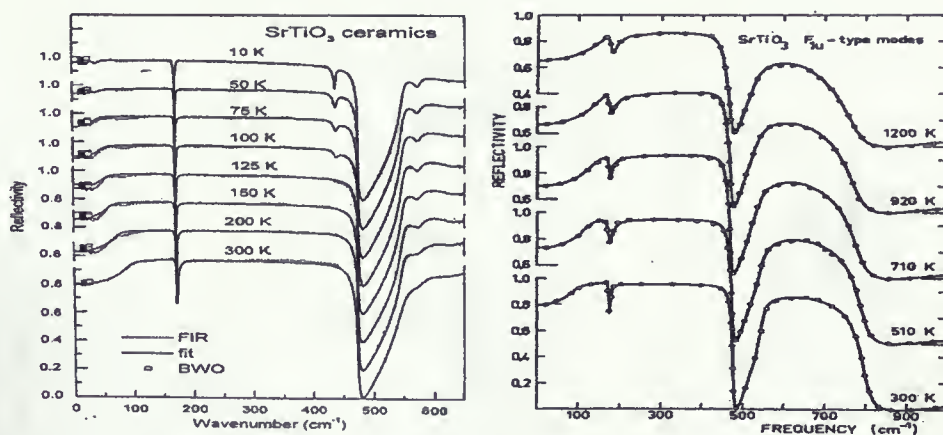


Figure 4.1: Previous reflectance work on SrTiO₃, from [25] (left) and [7] (right)

close to the reported structural transition temperature (roughly 105 K). After having recognized the noise present in the first set of measurements, approximately 1000 scans were performed for each of the intermediate ratios during the second set.

4.2.1 March 25 Measurements

On March 25, the sample was cooled to a temperature of roughly 10 K. Scans were taken on both the sample and the reference path. The sample temperature was subsequently raised to 150 K and 300 K, repeating the same procedure. After all measurements had been conducted on the sample, a thin gold film was deposited, and 300 K measurements were taken on the gold-coated sample. It was noted at this time that a layer of frost was covering parts of the Janis cryostat, indicating that its temperature had not yet stabilized. The following day, measurements were made on the gold-coated sample in the following order: 300 K, 10 K, 150 K, and 300 K. Results of the 300 K gold-coated intermediate ratios are shown in Figure 4.2. The measurements labelled as “Before Cooling” refer to the temperature sensor reporting a temperature of 300 K after having sat overnight, while “After Cooling” refers to 300 K measurements taken directly after the low-temperature measurements. An inset is provided, showing a magnified view of a region where a discrepancy is apparent. The concern was that not all the parts of the cryostat would be at the reported temperature. It has been determined that the differences between these spectra lie in slight changes to the position of

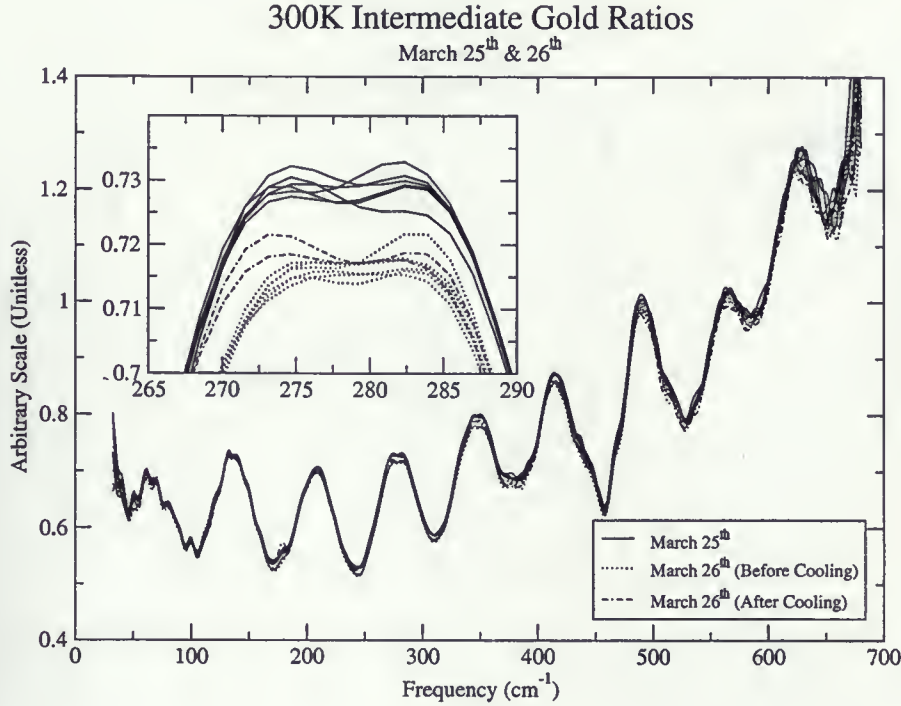


Figure 4.2: Comparison of the 300 K intermediate gold-coated sample ratios taken on separate days the sample during the time it takes for the Janis Cryostat to reach thermal equilibrium (due to thermal expansion). This process is known to take a great deal of time, sometimes requiring over 20 hrs. for room temperature to be achieved. It is believed that the sample holder is not returning to the same position each time.

To demonstrate the overall level of noise in the spectra, comparisons of the 300 K Reflectance (shown in Figure 4.3) illustrate data taken at different times. An expanded view of the spectra is provided as an inset, illustrating roughly a 1 % level of noise. Measurements were later made using roughly twice the number of scans which demonstrated a reduction in the amount of noise.

Figure 4.4 shows the unsmoothed, experimental reflectance results for 10, 150, and 300 K. From this data, strong agreement can be seen with the previous reflectance measurements. The overall appearance of the soft-mode is the same, as are the other two. This includes the emergence of the phonon mode near 440 cm⁻¹ associated with the cubic-tetragonal phase change at 110 K. As shown, the reflectance values still rose above 1 (by roughly 1 – 2 %) at several places for the lower

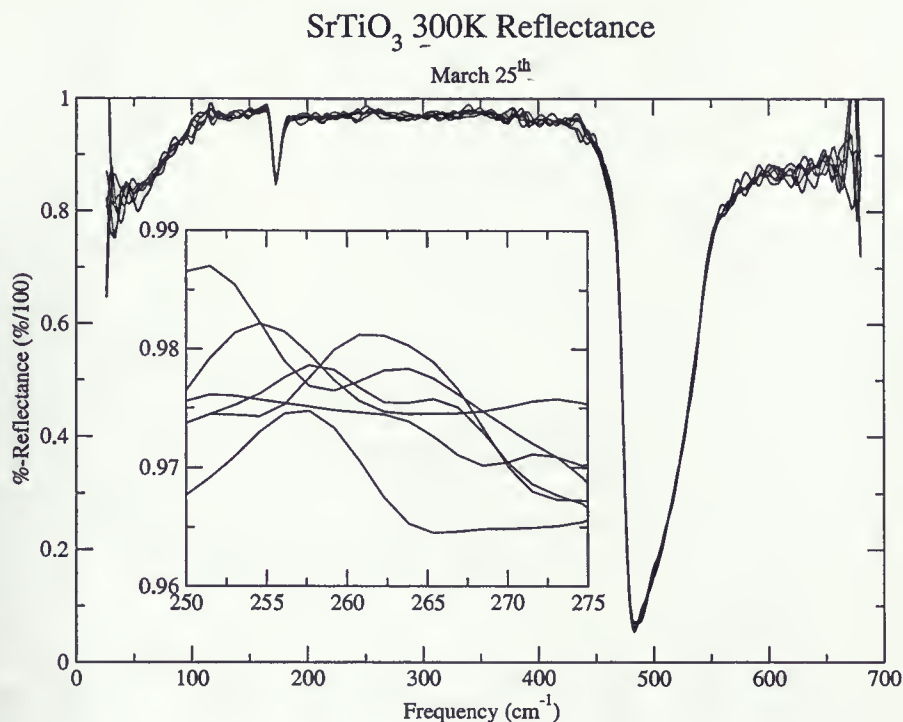


Figure 4.3: 300 K Reflectance measurements

temperatures, even after the resulting reflectance spectra were multiplied by 0.985 (the known reflectance of gold in this region). As this is a physical impossibility, it is believed that this is once again a result of thermal expansion.

4.2.2 June 10 Measurements

Measurements beginning on June 10 involved 1024 scans of both the sample and reference signals at 90 K, 125 K, 225 K. Additional measurements were performed at 300 K in order to allow for a correction factor to be applied. This proved useful, as the measured spectra for the absolute reflectance were well above unity (the results of a thin gold evaporation of poor quality). A frequency-dependent correction function, $C(\omega)$, was calculated from the 300 K reflectance spectra, $R(\omega)$, in the following

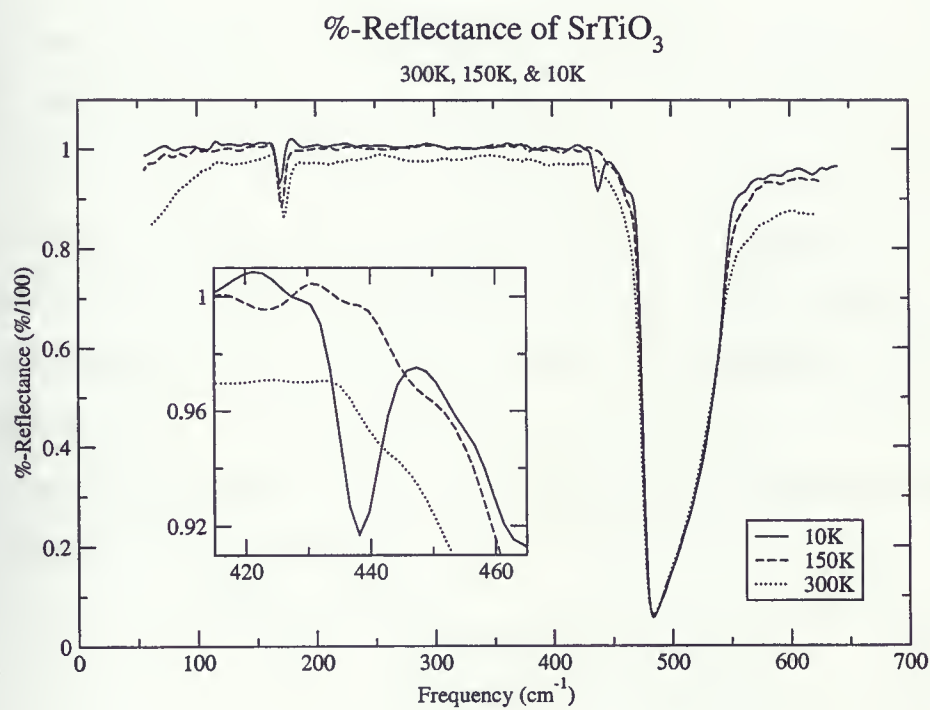


Figure 4.4: Reflectance results for 10, 150, and 300 K, showing a region (inset) of recent interest

way:

$$C(\omega) = \frac{R_{\text{March26,300K}}(\omega)}{R_{\text{June10,300K}}(\omega)}.$$

The corrected reflectance spectra, $R_{\text{corrected}}(\omega)$, were then calculated from:

$$R_{\text{corrected}}(\omega) = C(\omega) \times R_{\text{June10}}(\omega).$$

The March 25th and June 10th measurements are presented together in Figure 4.5. Note the presence of three high-reflectance regions (near 120, 300, and 600 cm^{-1}). A reflectance band is associated with each transverse optical mode (as shown in Figure 3.4). In addition, note the splitting seen near 440 cm^{-1} in the 10 K spectrum. This is associated with the cubic-tetragonal transition which had been previously observed by Petzelt et. al. in Figure 4.1 [25]. The final important feature is the temperature dependence of the reflectance for frequencies less than 150 cm^{-1} , due to the presence of a soft phonon mode.

Fits were made to the reflectance using initial parameters from previously published work in the factorized dielectric function of Equation 3.18.

$$\epsilon(\omega) = \epsilon_{\infty} \prod_j \frac{\Omega_{jLO}^2 - \omega^2 + i\gamma_{jLO}\omega}{\Omega_{jTO}^2 - \omega^2 + i\gamma_{jTO}\omega}. \quad (4.1)$$

The dielectric function was then broken into its real and imaginary parts ($\epsilon_1(\omega)$ and $\epsilon_2(\omega)$), which were used to calculate $n(\omega)$, $k(\omega)$, and $R(\omega)$. The parameters were adjusted by a least-squares fit to the reflectance data. Table 4.1 shows the values. The uncertainty reported normally ranged from 0.5 cm^{-1} to 1 cm^{-1} . Uncertainty in multi-parameter fits is difficult to estimate, so these uncertainty values may be low estimates. The reflectance spectra generated using these parameters, are compared to the experimental data from each temperature, in Figure 4.5. During the course of the fits, it was noticed that the soft-mode edge was not apparent in the 10 K, 90 K, and 125 K spectra, hence the values of Ω_{1TO} for these temperatures were fixed to the literature values from the

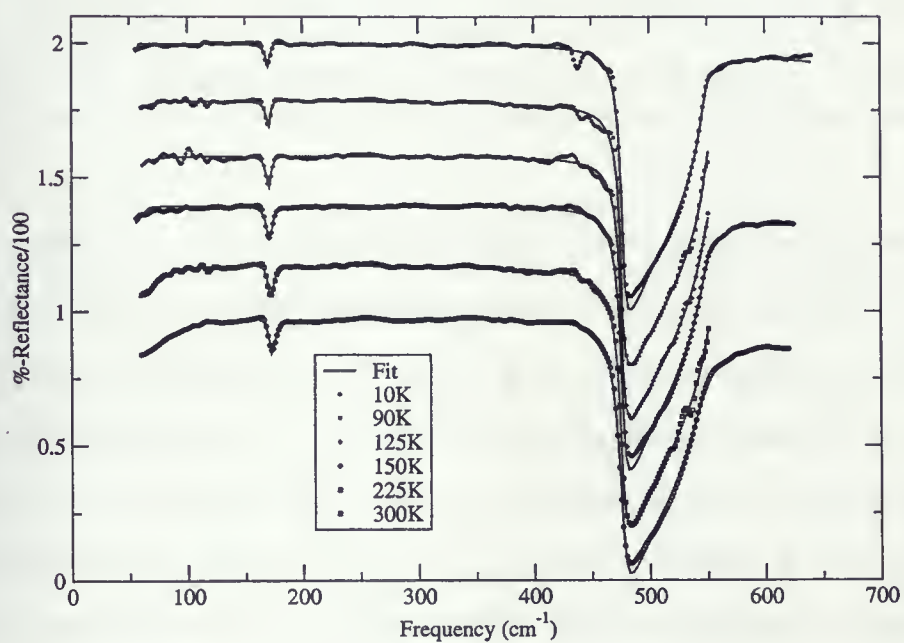


Figure 4.5: Summary of the collected reflectance data, showing the results of the theoretical fits. Adjacent spectra are shifted up by 20%.

	10K	90K	125K	150K	225K	300K
ϵ_{∞}	6.7	5.9	5.9	6.9	6.6	6.4
Ω_{1TO} (cm ⁻¹)	12.0**	45.0**	55.0**	64.0	83.6	94.3
γ_{1TO} (cm ⁻¹)	1.7	13.1	16.5	3.7	20.0	20.4
Ω_{1LO} (cm ⁻¹)	170.2	170.8	170.5	170.9	171.5	172.2
γ_{1LO} (cm ⁻¹)	4.1	4.0	4.7	5.8	4.9	5.5
Ω_{2TO} (cm ⁻¹)	171.1	171.8	172.0	173.1	173.4	174.5
γ_{2TO} (cm ⁻¹)	3.8	3.5	4.4	5.4	5.8	6.9
Ω_{2LO} (cm ⁻¹)	477.0	475.9	476.1	476.6	476.1	476.7
γ_{2LO} (cm ⁻¹)	3.5	3.1	3.6	4.2	4.6	7.0
Ω_{3TO} (cm ⁻¹)	547.1	550.5	549.7	547.9	551.7	544.2
γ_{3TO} (cm ⁻¹)	7.7	6.0	10.6	10.9	9.9	21.0
Ω_{3LO} (cm ⁻¹)	796.0*	796.0*	796.0*	796.0*	796.0*	796.0*
γ_{3LO} (cm ⁻¹)	18.0*	18.0*	18.0*	26.0*	26.0*	26.0*

Table 4.1: Parameters found during fits of the factorized dielectric function. Some of the parameters were fixed to values reported by Fleury and Worlock (**) [23] and Servoin et al (*) [7].

Raman measurements of Fleury and Worlock (**) [23]. For the same reason, the highest frequency phonon modes Ω_{3TO} and γ_{3LO} values were fixed at those determined by Servoin et al (*) [7].

The overall physical appearance of the spectra in Figure 4.5 are consistent with the previously measured data shown in Figure 4.1. As expected, the frequency of the soft mode decreases with temperature. A plot of the relationship between the frequency of the soft mode and temperature was made, and compared with other workers results. As shown in Figure 4.6, the three experimentally determined frequencies for 300 K, 225 K, and 150 K were in reasonable agreement with previous measurements. Note that Cowley's data is from neutron scattering, while Fleury and Worlock made Raman measurements. Absent from this plot, are the three temperatures (125 K, 90 K, and 10 K) for which there is not enough low frequency data with which to adequately determine Ω_{1TO} .

The onset of the structure below 110 K situated near 440 cm⁻¹ in Figure 4.5 is not quite as strong as shown in previous work. The relative size of the structure appears larger (at a given temperature) in literature. Due to the noise present in the 90 K spectra, it is difficult to discern the structure. This excess noise is present due to multiplication by the correction function, $C(\omega)$. Another possible reason for the lack of structure may be explained as follows. Recent studies have

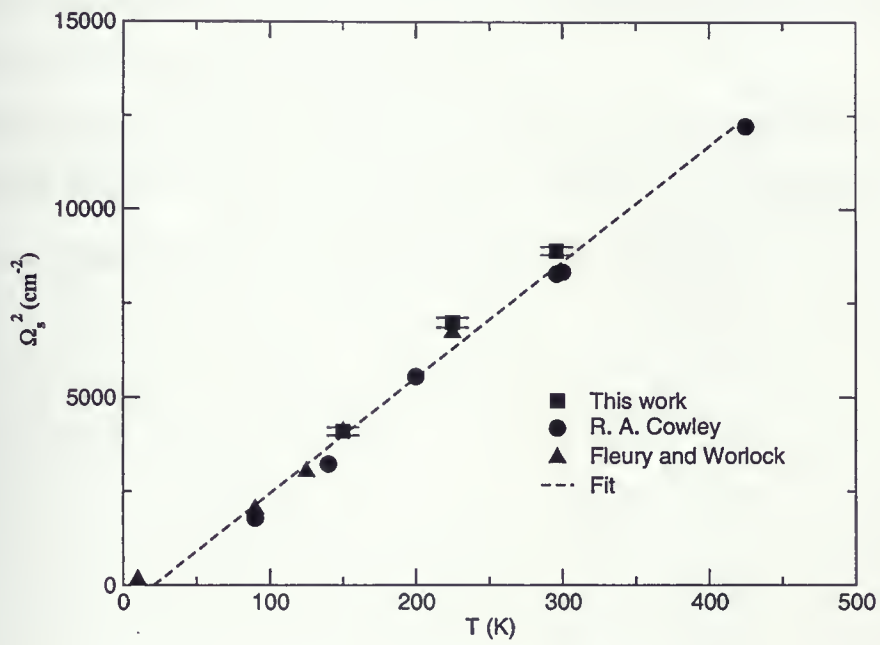


Figure 4.6: Plot of Ω_s^2 vs. T for the experimentally determined points

shown a relatively wide range of T_c values for the structural phase transition. Hünnefeld et al had shown that based on the method of crystal growth (float-zone, flux, or Verneuil grown), the transition temperature can vary over a range of roughly 98.7 K to 105.8 K [26]. An argument could be made that the sample used may be of the variety that goes through a structural phase transition at the lower end of the scale. At the time of experimentation, it was expected that the transition temperature was very nearly 110 K. While this still leaves approximately 9 K unaccounted for, it should also be kept in mind that there is probably a temperature gradient between the temperature sensor and the sample mount. This, coupled with the slow response of the cryostat to variations in temperature may explain the discrepancies. One crucial improvement to the system will be to mount a temperature sensor closer to the sample.

A careful examination of Figure 4.6 will reveal that all of the experimentally collected points fall to the left of the line of best fit. This indicates that the temperatures being reported by the sensor are in fact lower than the actual temperature of the sample.

Chapter 5

Conclusions

A reflectance spectrometer was successfully constructed utilizing a Brüker IFS 66v/S spectrometer, Janis Industries sample cryostat, and IR Labs bolometer. The system was designed to have a working frequency range of $60 - 670 \text{ cm}^{-1}$ while maintaining sample temperatures from 4.2 K to 325 K. Ultra-high vacuum components were utilized for the construction of the sample chamber. These allowed for an ultimate pressure of roughly 4×10^{-8} Torr. At this stage, reuseable rubber CF flange gaskets are utilized. It is expected that through the use of copper CF gaskets and “baking” of the system, the vacuum could be improved. In addition, the polypropylene window (0.003” thick) was believed to be a slow vacuum leak. Use of a thicker polyethylene window may help achieve lower pressures. For other beamsplitter/detector pairs, more solid windows (such as CaF_2) may act as a better barrier against this leakage.

Tests of the system were performed using the highly-ionic and dielectric SrTiO_3 . As this material had been highly studied in the past it was known to undergo a structural phase transition in between 98.7 K and 105.8 K. Direct reflectance measurements of the sample effectively showed the splitting of a phonon mode near 440 cm^{-1} and below 110 K. This splitting was associated with the change from a cubic to tetragonal perovskite structure.

A characteristic of SrTiO_3 is that it exhibits a temperature-dependent “soft-mode” behaviour. Much work has been done in the past, supporting the connection between the Lyddane-Sachs-Teller relation and the incipient ferroelectric behaviour. This was confirmed in the present measurements through the temperature dependence of the soft-mode frequency. Once again however, the data indicates that the sample temperature was not quite as low as was being reported by the temperature sensor within the Janis cryostat. It is suggested that either a temperature sensor be mounted closer

to the sample, or the sample be provided with better thermal contact to the cold-finger.

Noise was apparent at the highest and lowest frequencies in the reflectance spectra. This precluded any attempts to fit the soft mode frequency of the factorized dielectric function at lower temperatures. It is suggested for all future work that a minimum of 1000 scans per intermediate ratio be conducted, as the signal-to-noise ratio should improve accordingly.

With all of the above considerations in mind, the system can be used to conduct research reliably on new materials.

Bibliography

- [1] K. A. Muller and W. Berlinger. Characteristic structural phase transition in perovskite-type compounds. *Phys. Rev. Lett.*, 21(12):814 – 817, 1968.
- [2] R. Blinc and B. Žekš. *Soft Modes in Ferroelectrics and Antiferroelectrics*. American Elsevier Publishing Company, New York, 1974.
- [3] Matthew Trainer. Ferroelectricity: Measurement of the dielectric susceptibility of strontium titanate at low temperatures. *Am. J. Phys.*, 69(9):966 – 969, 2001.
- [4] R. A. Cowley. Lattice dynamics and phase transitions of strontium titanate. *Phys. Rev.*, 134(4A):A981 – A997, 1964.
- [5] K. A. Müller. SrTiO₃: An intrinsic quantum paraelectric below 4 K. *Phys. Rev. B*, 19(7):3593 – 3602, 1979.
- [6] K. Kamarás et al. The low-temperature infrared optical functions of SrTiO₃ determined by reflectance spectroscopy and spectroscopic ellipsometry. *J. Appl. Phys.*, 78(2):1235 – 1240, 1995.
- [7] Y. Luspin J. L. Servoin and F. Gervais. Infrared dispersion in SrTiO₃ at high temperature. *Phys. Rev. B*, 22(11):5501 – 5506, 1980.
- [8] F. J. Owens and C. P. Poole. *The New Superconductors*. Plenum, New York, 1996.
- [9] C. S. Koonce and Marvin L. Cohen. Superconducting transition temperatures of semiconducting SrTiO₃. *Phys. Rev.*, 163(2):380 – 390, 1967.

-
- [10] *Bruker IFS 66v/S User's Manual*. Bruker Optik GmbH, 1998.
- [11] *Infrared Laboratories, Systems Catalog*. Infrared Laboratories, Inc., 1993.
- [12] G. Chanin and J. P. Torre. He³ refrigerators and bolometers for infrared and millimeter wave observations. In K. J. Button, editor, *Infrared and Millimeter Waves*, volume 10, Orlando, 1983. Academic Press.
- [13] G. Chanin and J. P. Torre. *Infrared and Millimeter Waves*, volume 10.
- [14] K. D. Möller and W. G. Rothschild. *Far-Infrared Spectroscopy*. Wiley-Interscience, New York, 1971.
- [15] R. J. Bell. *Introductory Fourier Transform Spectroscopy*. Academic Press, New York, 1972.
- [16] C. Kittel. *Introduction to Solid State Physics 7th Edition*. John Wiley & Sons, New York, 7 edition, 1996.
- [17] <http://www.wavemetrics.com>.
- [18] F. Wooten. *Optical Properties of Solids*. Academic Press, New York, 1972.
- [19] W. G. Spitzer et al. Far infrared dielectric dispersion in BaTiO₃, SrTiO₃, and TiO₂. *Phys. Rev.*, 126(5):1710 – 1721, 1962.
- [20] Dwight W. Berreman and F. C. Unterwald. Adjusting poles and zeros of dielectric dispersion to fit restrahlen of PrCl₃ and LaCl₃. *Phys. Rev. B*, 19(7):3593 – 3602, 1979.
- [21] R. H. Lyddane R. G. Sachs and E. Teller. On the polar vibrations of alkali halides. *Phys. Rev.*, 59:673 – 676, 1941.
- [22] A. S. Barker, Jr. Temperature dependence of the transverse and longitudinal optic mode frequencies and charges in SrTiO₃ and BaTiO₃. *Phys. Rev.*, 125(5):1527 – 1530, 1962.

-
- [23] P. A. Fleury and J. M. Worlock. Electric-field-induced raman scattering in SrTiO_3 and KTaO_3 . *Phys. Rev.*, 174(2):613 – 623, 1968.
- [24] S. Tajima et al. Infrared reflectivity and electronic states in perovskite-type oxides $\text{La}_{1-x}\text{Sr}_x\text{FeO}_3$ and $\text{La}_{1-x}\text{Sr}_x\text{CoO}_3$. *J. Phys. C: Solid State*, 20:3469 – 3484, 1987.
- [25] J. Petzelt et al. Polar grain boundaries in undoped SrTiO_3 ceramics. *Journal of the European Ceramic Society*, 21:2681 – 2686, 2001.
- [26] H. Hünnefeld et al. Influence of defects on the critical behavior at the 105 K structural phase transition of SrTiO_3 : On the origin of the two length scale critical fluctuations. *Phys. Rev. B*, 19(7):3593 – 3602, 1979.

4567-25

